LETTER

https://doi.org/10.1038/s41586-019-1159-6

Subthreshold firing in Mott nanodevices

Javier del Valle[1]*, Pavel Salev[1], Federico Tesler[2,3], Nicolás M. Vargas[1], Yoav Kalcheim[1], Paul Wang[1], Juan Trastoy[1,4], Min-Han Lee[1], George Kassabian[1], Juan Gabriel Ramírez[5], Marcelo J. Rozenberg[6] & Ivan K. Schuller[1]

Resistive switching, a phenomenon in which the resistance of a device can be modified by applying an electric field[1–5], is at the core of emerging technologies such as neuromorphic computing and resistive memories[6–9]. Among the different types of resistive switching, threshold firing[10–14] is one of the most promising, as it may enable the implementation of artificial spiking neurons[7,13,14]. Threshold firing is observed in Mott insulators featuring an insulator-to-metal transition[15,16], which can be triggered by applying an external voltage: the material becomes conducting ('fires') if a threshold voltage is exceeded[7,10–12]. The dynamics of this induced transition have been thoroughly studied, and its underlying mechanism and characteristic time are well documented[10,12,17,18]. By contrast, there is little knowledge regarding the opposite transition: the process by which the system returns to the insulating state after the voltage is removed. Here we show that Mott nanodevices retain a memory of previous resistive switching events long after the insulating resistance has recovered. We demonstrate that, although the device returns to its insulating state within 50 to 150 nanoseconds, it is possible to re-trigger the insulator-to-metal transition by using subthreshold voltages for a much longer time (up to several milliseconds). We find that the intrinsic metastability of first-order phase transitions is the origin of this phenomenon, and so it is potentially present in all Mott systems. This effect constitutes a new type of volatile memory in Mott-based devices, with potential applications in resistive memories, solid-state frequency discriminators and neuromorphic circuits.

Certain Mott systems exhibit a first-order insulator-to-metal transition (IMT) across which the resistivity changes by several orders of magnitude[15,16]. This transition can be induced not only by temperature, but also by applying an electric field. In recent years, this voltage-triggered IMT has become a topic of great interest[10,12,17,18] as it opens the possibility of switching the device between two very well defined states: 'off' (insulating) and 'on' (conductive). This type of threshold switching makes Mott materials ideal candidates for neuromorphic devices[13,14] or voltage selectors in resistive (re-)RAM memories[7,19]. This has motivated much research aimed at understanding the voltage-triggered IMT. Topics such as its underlying mechanism[10,12,17], its characteristic timescales[10,18] and its filamentary nature[12,13,20] have been thoroughly studied. Despite all this research, an important issue must still be addressed: how does the system return to its insulating state after the voltage is removed? Understanding this is crucial, as read/write processes in memory applications can take place at very high rates. How the device recovers from a previous pulse before the next one arrives could have profound implications for device design and reliability. On a more fundamental level, studying this recovery provides an opportunity to understand relaxation dynamics in first-order phase transitions[21]. Metastability and phase coexistence in first-order phase transitions create substantially more complex dynamics than those found in second-order transitions[21]. Whereas optical pump–probe experiments have allowed IMTs to be monitored in the femtosecond and picosecond timescales[22,23], relaxation back into the insulating state is a much slower process[24,25], which is difficult to study using this technique. Resistive switching offers an alternative approach: exciting the system with a voltage-triggered transition and monitoring the recovery process afterwards. This provides a local probing technique, which is able to capture the evolution of the system over a broad temporal range, from nanoseconds to minutes.

To address these questions, we have studied the dynamic response of VO_2 and V_2O_3 nanodevices subjected to voltage pulses. Figure 1a shows a scanning electron microscope (SEM) image of one of the devices: a VO_2 thin film, on top of which two Ti/Au electrodes were patterned. The small electrode separation (around 100 nm) allows application of a very high electric field (about 10 MV m^{-1}) using just a few volts. The devices feature an IMT around 340 K for VO_2 (Fig. 1b) and 145 K for V_2O_3 (Extended Data Fig. 1a). To characterize the dynamic response of the device, we use a function generator to apply voltage pulses and a broadband oscilloscope to monitor the current flowing through the device (Fig. 1a).

Figure 1c shows the current as a function of time when 200-ns voltage pulses are applied to the VO_2 device at $T = 330$ K. The blue and red curves show the response to two pulses of different amplitude: 1.60 V and 1.70 V. The stark difference between them illustrates the sharp threshold character of the electrically induced IMT: the device remains insulating throughout the whole 1.60-V pulse, but becomes conducting when a slightly higher pulse (1.70 V) is applied. This behaviour is quantified in the inset of Fig. 1c, where the probability of triggering the IMT (P_{Trigger}) as a function of the pulse amplitude (V_{Applied}) shows a step-like behaviour around $V_{\mathrm{Threshold}} = 1.65$ V. The sharpness of the step is such that $P_{\mathrm{Trigger}} = 0$ below a voltage $V = 0.97\ V_{\mathrm{Threshold}}$ and $P_{\mathrm{Trigger}} = 1$ above $V = 1.02\ V_{\mathrm{Threshold}}$. V_2O_3 devices feature a similar behaviour (Extended Data Fig. 1b).

To determine how fast the system returns to its insulating state once the pulse ends, we monitor the resistance (R) as a function of time. In Fig. 1d we plot R and V_{Applied} as functions of time. The device does not immediately become insulating: R remains close to its low-resistance value for about 75 ns (t_{Off}; marked with an orange arrow) before rising abruptly. This sudden resistance change can be identified as the metal-to-insulator phase transition onset, and t_{Off} can be considered as the characteristic time for the 'on' to 'off' switching. This t_{Off} provides an upper bound for the time it takes the device to cool down below the transition temperature.

We used a software simulator (COMSOL Multiphysics) to estimate the cool-down time. Similarly to the experiment, we obtained cooling times of the order of tens of nanoseconds. Figure 1e displays the simulated t_{Off} as a function of the base temperature (T), showing that it increases with temperature, but remains in the 10^{-7} s range for all temperatures. Although monitoring the resistance is useful to determine this cooling time, the dependence of resistance on percolation makes it insensitive to the presence of small isolated metallic domains once the conduction path is broken. Instead, the threshold voltage is a more sensitive probe with which to study the relaxation dynamics beyond t_{Off}.

To investigate how the system relaxes beyond its characteristic thermal timescale, we use an electric transport pump–probe procedure, as depicted in Fig. 2a. We first excite (pump) the VO_2 using a voltage pulse

[1]Center for Advanced Nanoscience, Department of Physics, University of California–San Diego, La Jolla, CA, USA. [2]Departamento de Física, FCEyN, Universidad de Buenos Aires, Buenos Aires, Argentina. [3]IFIBA, Conicet, Ciudad Universitaria, Buenos Aires, Argentina. [4]Unité Mixte de Physique, CNRS, Thales, Université Paris-Sud, Université Paris-Saclay, Palaiseau, France. [5]Departamento de Física, Universidad de los Andes, Bogotá, Colombia. [6]Laboratoire de Physique des Solides, CNRS, Université Paris-Sud, Université Paris-Saclay, Orsay, France. *e-mail: jdelvallegranda@ucsd.edu

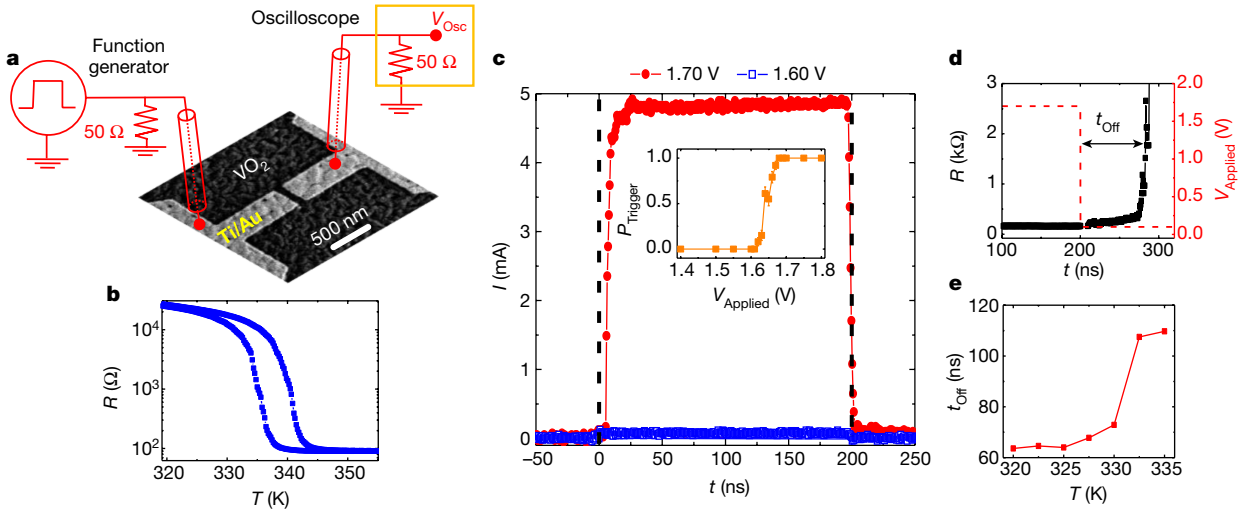

Fig. 1 | Voltage-triggered IMT and cooling time. a, SEM image of the VO_2 device and schematic representation of the measurement setup. The Ti (20 nm)/Au (30 nm) electrodes are light grey, whereas the VO_2 underneath is shown in a dark tone. **b**, Resistance of the device versus temperature. Both the cooling and heating branches are shown. **c**, Current versus time at $T = 330$ K, when two voltage pulses with different amplitudes are applied: 1.60 V (blue open squares) and 1.70 V (red filled circles). The duration of the pulse (marked with vertical dashed lines) is 200 ns. Inset, probability of triggering the IMT as a function of the pulse amplitude. This probability was obtained by observing how many times the IMT was triggered in 100 pulses. The error bars were calculated using the standard deviation of the binomial distribution. **d**, Applied voltage (right axis, red dashed line) and resistance (left axis, black filled squares) versus time at $T = 330$ K, after the application of a 200-ns voltage pulse. **e**, Simulated time t_{Off} versus temperature (see Methods).

with amplitude $V_{Pump} = 1.25\ V_{Threshold}$, so the IMT is triggered. We then wait for the system to relax for a certain delay time (τ), before sending a second (probe) pulse with (subthreshold) amplitude $V_{Probe} < V_{Threshold}$. This second pulse should not trigger the IMT. However, as Fig. 2b shows, the probe pulse does trigger the device, in this case with a voltage amplitude of just $V_{Probe} = 0.6\ V_{Threshold}$. This value is much lower than the threshold voltage, and is in stark contrast to the behaviour shown in the inset of Fig. 1c. This result implies that the device keeps a 'memory' of the previous firing event, which allows it to fire again with subthreshold pulses. We note that in the case of Fig. 2b, the time τ between the two pulses is 100 μs, which is three orders of magnitude larger than t_{Off}, and around five orders of magnitude larger than the RC constant of the circuit. This means that a new, much slower memory mechanism is at play.

To investigate further the characteristic time for this memory, we perform this pump–probe experiment and change the separation τ between pump and probe. Figure 2c shows the probability for the probe pulse to fire the device as a function of τ, for different amplitudes of V_{Probe}. As expected, the probability decreases as τ is increased, but it does so in a slow way, spanning several decades in time up to the millisecond range. By defining $\tau_{50\%}$ as the delay time for which the firing probability is down to 50%, we can provide a quantitative description of the temperature dependence of the memory effect. Figure 2d shows $\tau_{50\%}$ as a function of T, for $V_{Probe} = 0.6\ V_{Threshold}$. This memory effect is markedly enhanced as the temperature is increased, diverging at the transition temperature, T_{IMT} (note that the y axis is on a logarithmic scale). Similar results were observed in V_2O_3 (Extended Data Fig. 2). We note that $V_{Threshold}$ and the insulating state resistance remained unchanged after more than 10^8 firing events, ruling out device degradation or defect creation as being responsible for the effect.

The divergence of $\tau_{50\%}$ close to T_{IMT} is a clear sign that this effect is related to the dynamics of the phase transition. Similar results were obtained for VO_2 and V_2O_3, suggesting that the underlying mechanism must be rather general and not dependent on the particular details of each material. One possibility is that long-lived metallic domains remain trapped in a metastable state. They would persist in the device long after the switching event, acting as 'seeds' that facilitate the triggering of the IMT with subthreshold voltages. The existence of such persistent domains has been suggested by electric transport[24,25] and pump–probe[23] studies. To test this hypothesis, it is necessary to directly monitor the amount of metallic domains as a function of time. Optical reflectivity is a very sensitive probe of the amount of metallic domains in the device due to the large changes in optical constants between the insulating and metallic states[26]. Figure 3b shows the evolution of the reflectivity (denoted by ρ), measured with a 660-nm laser, as temperature is ramped across the IMT in a VO_2 thin film. Using time-dependent reflectivity measurements, we monitored how metallic domains, which form during an electrical pulse, relax to the insulating phase after the pulse is turned off.

Figure 3a shows the experimental setup used to measure optical reflectivity while performing resistive switching. The laser is focused on a VO_2 gap between two metallic electrodes, separated by 10 μm. The IMT is triggered by current pulses while ρ is recorded as a function of time. Figure 3c shows the voltage and reflectivity dependence as a d.c. current is ramped up across the gap: ρ starts decreasing once the IMT is triggered, and keeps decreasing as the current is increased. This is to be expected, as the metallic domains are arranged in a filamentary structure whose size will be proportional to the current. We note that the laser spot size (about 5 μm) is larger than the filament size, accounting for the smaller change in reflectivity compared to that observed when the entire probed region is metallic. To take this into account, we define the normalized reflectivity $\rho_{Norm} = (\rho - \rho_{On})/(\rho_{Insulator} - \rho_{On})$, where $\rho_{Insulator}$ and ρ_{On} are respectively the reflectivity before and during the pulse. To investigate the relaxation dynamics, we send current pulses and measure the evolution of ρ_{Norm} once the current stops. Such a measurement is presented in Fig. 3d: ρ_{Norm} is low while the current is passing through the gap, and returns to the insulating-phase value at $t = 0$, the moment the current is turned off. A closer inspection reveals that reflectivity does not completely return to its initial high value. Instead, it approaches it in an asymptotic way in a relaxation process that is not complete even after 10 ms, confirming the presence of persistent, long-lived domains. The amount of such metallic domains is proportional to $(1 - \rho_{Norm})$. Figure 3e displays a log–log plot of $(1 - \rho_{Norm})$ against time for different temperatures. All curves show a remarkable power-law dependence that can be fitted to $(t/\tau_\rho)^{\alpha}$, with $\alpha \approx 0.5$–0.6. Note that τ_ρ is not a characteristic timescale, as it can be taken out of the parentheses as a constant.

Such power-law behaviour explains the absence of a characteristic timescale and the observation of subthreshold firing for several decades in time. This type of relaxation is observed in a wide range of physical

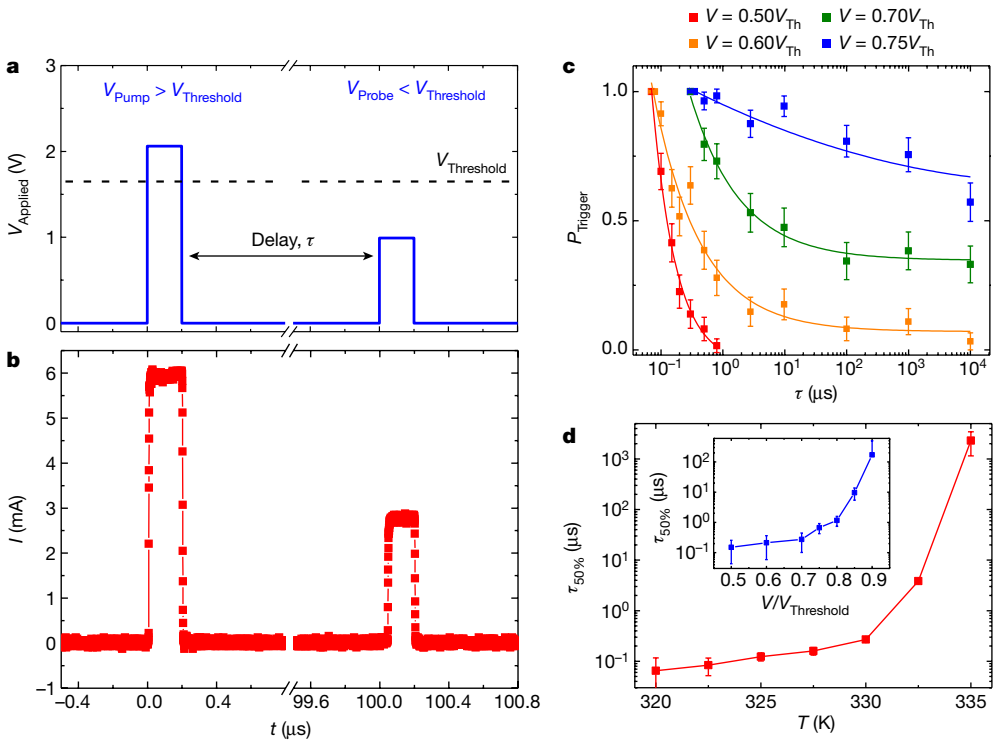

Fig. 2 | Subthreshold firing and memory effect in VO_2. a, Applied voltage as a function of time. A pump–probe procedure is followed: a super-threshold pulse is first applied to trigger the IMT, followed by a subthreshold probe pulse, after a delay time τ. **b**, Current versus time at $T = 330$ K, when the voltage shown in **a** is applied. There is a delay $\tau = 100$ μs between the two pulses. **c**, Probability that the probe pulse will trigger the IMT ($P_{Trigger}$) as a function of τ, at $T = 332.5$ K. $P_{Trigger}$ is plotted for different V_{Probe} amplitudes: $0.5V_{Th}$, $0.6V_{Th}$, $0.7V_{Th}$ and $0.75V_{Th}$ (where V_{Th} indicates $V_{Threshold}$). This probability was obtained after averaging 100 pump–probe protocols at each τ. The error bars were calculated using the standard deviation of the binomial distribution. Between pump–probe experiments, the system was allowed to relax for several seconds to ensure complete relaxation. Solid lines are fits to curves of the type $\alpha t^{-\beta} + \gamma$, where α, β and γ are fitting parameters obtained by the least-squares method. **d**, Delay time at which the firing probability is 50% ($\tau_{50\%}$) plotted against T, for a 0.6 $V_{Threshold}$ amplitude pulse. Inset, plot of $\tau_{50\%}$ versus $V_{Probe}/V_{Threshold}$, at $T = 330$ K. $\tau_{50\%}$ was calculated using the fitting curves shown in **c**. Error bars were derived by uncertainty propagation, using the standard error of the fit.

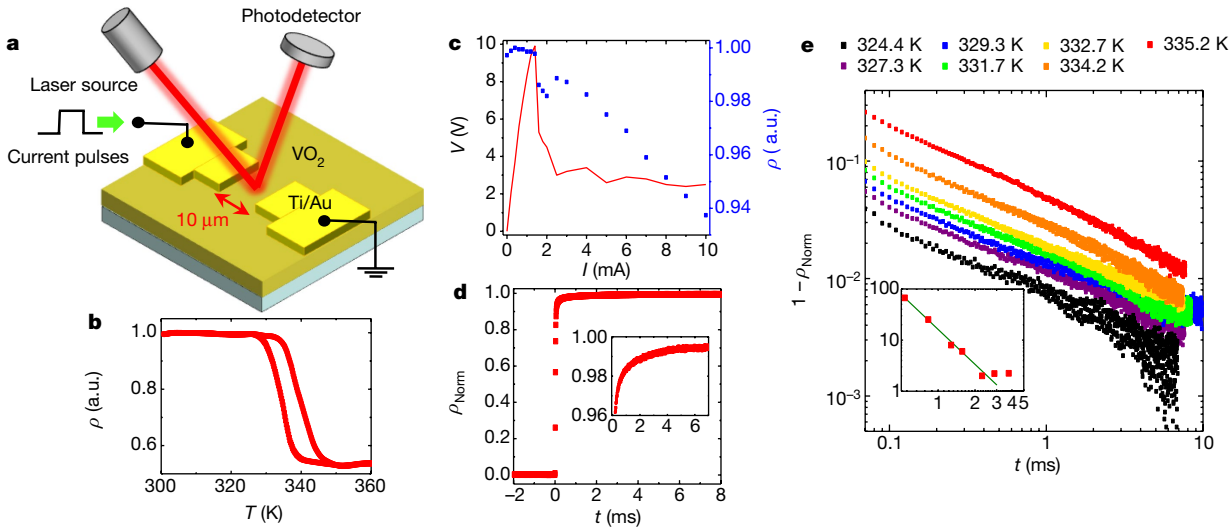

Fig. 3 | Metal-to-insulator relaxation dynamics from reflectivity. **a**, Experimental setup used for optical reflectivity experiments. A 660-nm laser probes the temporal evolution of the reflectivity in the sample. The laser is focused on a 10-μm VO_2 gap (brown) between two Ti/Au electrodes (yellow). Current pulses are sent to induce the voltage-triggered IMT. **b**, Reflectivity (ρ) versus temperature in a VO_2 film. **c**, Voltage (left axis, red line) and reflectivity (right axis, blue squares) as a function of the current through the VO_2 device. The measurements were done at $T = 329.3$ K. **d**, Normalized reflectivity $\rho_{Norm} = (\rho - \rho_{On})/(\rho_{Insulator} - \rho_{On})$ as a function of time at 331.7 K. A 10-mA current flows through the VO_2 device for $t < 0$, dropping to 0 mA at $t = 0$. Data at $t > 0$ show the relaxation process back into the insulating state. Inset, zoom with an expanded y axis into the relaxation process (the axis variables are the same as in the main panel). **e**, Plot on log–log scales of $1 - \rho_{Norm}$ versus t at various temperatures (see key) as a function of time, for a VO_2 device. Current is turned off at $t = 0$. Inset, τ_ρ (y axis) versus $(1 - T/T_C)$ (x axis) on a log–log plot, using $T_C = 337.0$ K.

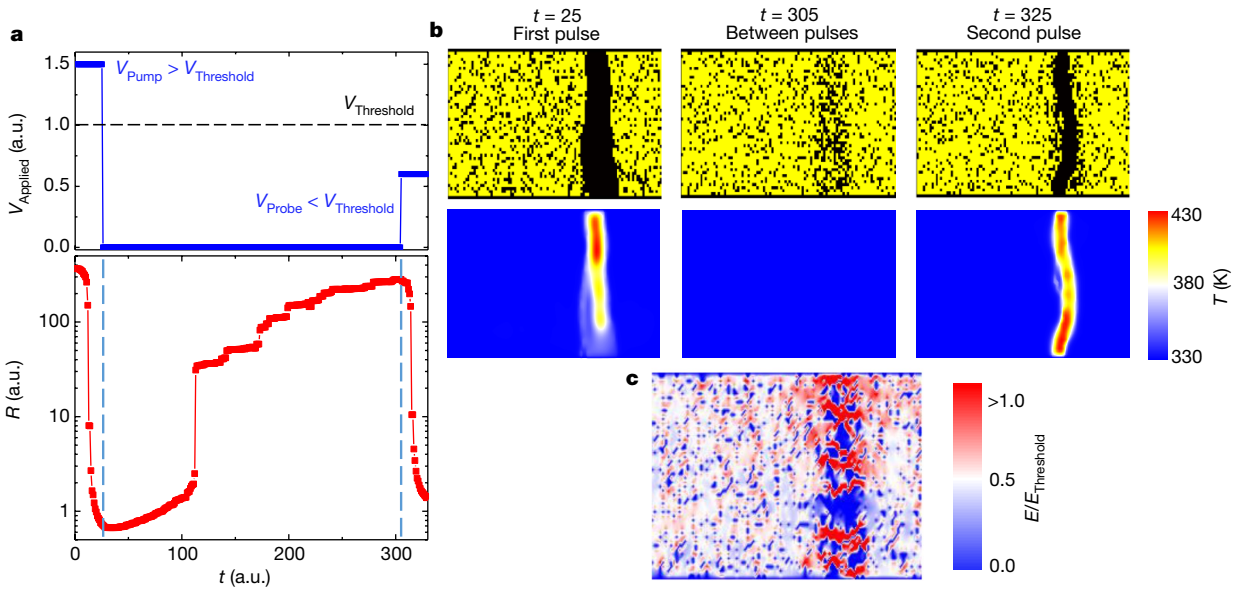

Fig. 4 | Simulations of subthreshold triggering and persistent domains in VO_2. a, Top, applied voltage versus time as used in the resistor network simulations. A pump–probe procedure similar to that used in the experiments, with a super-threshold pulse followed by a subthreshold one, is used. Bottom, the simulated resistance of the device (R) versus time, with vertical blue dotted lines signalling the beginning and end of the pulses. **b**, Top row, simulated 2D distribution of metallic (black) and insulating (yellow) domains at three different times: during the first pulse ($t = 25$ simulation steps), just before the second pulse ($t = 305$ simulation steps) and during the second pulse ($t = 325$ simulation steps). Bottom row, simulated 2D temperature distribution at the same three times. The base temperature in the simulation is $T = 338$, while $T_C = 340$. **c**, Simulated 2D distribution of the normalized electric field intensity (colour scale) just after the second pulse is applied ($t = 305$ simulation steps). The electric field intensity is normalized to the threshold electric field, defined as $E_{Threshold} = V_{Threshold}/d$, where d is the distance between the electrodes.

phenomena in which strain coupling creates different activation energies in each domain, leading to very different individual relaxation rates[27–30]. Such a scenario is very likely to happen in VO_2 and V_2O_3, which have a structural phase transition concomitant with the IMT[15]. Strain has been shown to play a major role in domain configuration and dynamics[16]. Fractal-like domain formation, with structure sizes across all length scales, have been reported in VO_2 films[31]. Such structures would inherently display scale-less relaxation dynamics similar to the ones we observed. Moreover, multiscale avalanche sizes have been previously reported[32] across the IMT in VO_2.

It must be noted that the fitting parameter τ_ρ is temperature dependent, becoming larger and causing slower dynamics as the temperature increases. In the inset of Fig. 3e we show τ_ρ versus $(1 - T/T_C)$ on a log–log scale, with $T_C = 337.0$ K being the middle point of the VO_2 IMT. The data fit a straight line, yielding a critical scaling behaviour characteristic of phase transitions: $\tau_\rho \propto (1 - T/T_C)^{\nu}$. First-order phase transitions (such as some IMTs) can also display critical dynamics, a phenomenon known as super-critical or pseudo-critical slowing down[21]. This effect mimics the criticality observed in second-order transitions and could explain why criticality has been recently observed near T_C in VO_2 (ref. [33]) and in charge-ordered ferrites[34]. We note the similarities between our transport and reflectivity measurements: (i) both exhibit relaxation dynamics that extend for several decades in time ($P_{Trigger}$ versus ρ); and (ii) their dynamics slow down with increasing temperature, diverging at T_C (τ_ρ versus $\tau_{50\%}$). These similarities are a clear indication that persistent metallic domains are indeed responsible for the memory effect observed in the transport properties.

To understand how persistent domains affect the IMT triggering, we performed resistor network simulations in which each site can be either metallic or insulating[13]. The IMT can be locally triggered at each site of the network by Joule heating and the relaxation dynamics are determined from a Landau free energy functional. Figure 4a presents the time evolution of the applied voltage, $V_{Applied}$, and the resistance of the VO_2 gap, R. A similar protocol to the experimental one is followed: a voltage pulse above $V_{Threshold}$ triggers the IMT, followed by a probe pulse of 0.6 $V_{Threshold}$ after some delay time. In good agreement with experiments, the simulation shows that the transition can be re-triggered by a subthreshold voltage pulse. Figure 4b (top row) shows the two-dimensional (2D) distribution of metallic and insulating sites at different simulation times (given in units of simulation steps): $t = 25$, 305 and 325, that is, during the first pulse, just before the second pulse and during the second pulse. The voltage-triggered IMT occurs through an emergent filamentary structure ($t = 25$) with the metallic regions forming conductive channels[12,20]. Once the voltage is removed, the system cools below T_C and the resistance abruptly increases as most domains rapidly relax.

However, the resistance does not fully recover as some residual domains still remain within the insulating matrix ($t = 305$). The mechanism by which these regions facilitate the re-triggering of the IMT can be understood by considering the 2D electric field distribution. Figure 4c shows this distribution just after the second pulse is applied ($t = 325$): the presence of metallic inclusions creates an inhomogeneous field distribution. The electric field in the insulating boundaries between metallic inclusions is greatly enhanced due to a field-focusing effect similar to that of lightning rods. This enhancement is enough to generate electric fields above $E_{Threshold}$ (defined as $V_{Threshold}/d$, with d being the electrode separation), locally triggering the IMT and starting a filament formation process that results in subthreshold firing. We note that our simulations do not account for strain coupling and thus cannot reproduce the power-law temporal relaxation. However, they are useful in demonstrating that residual metallic regions can induce subthreshold firing (see Supplementary Video) and predicting that the dynamics slow down as T approaches T_C.

Our work shows a new type of volatile memory in Mott nanodevices that can last several orders of magnitude longer than the cooling time of the device. Subthreshold firing might open up numerous new functionalities in these systems, such as low-energy volatile memory, solid-state frequency filtering (discussed in Methods and shown in Extended Data Fig. 3) or time-dependent plasticity in neuromorphic computing[6,7]. Conversely, this effect must be taken into account when considering

their implementation as voltage switches, as it might limit their read/write speed and reliability[7,19].

Online content

Any methods, additional references, Nature Research reporting summaries, source data, statements of data availability and associated accession codes are available at https://doi.org/10.1038/s41586-019-1159-6.

Received: 2 August 2018; Accepted: 6 February 2019;
Published online 1 May 2019.

1. Beck, A., Bednorz, J. G., Gerber, Ch., Rossel, C. & Widmer, D. Reproducible switching effect in thin oxide films for memory applications. *Appl. Phys. Lett.* **77**, 139 (2000).
2. Waser, R. & Aono, M. Nanoionics-based resistive switching memories. *Nat. Mater.* **6**, 833–840 (2007).
3. Strukov, D. B., Snider, G. S., Stewart, D. R. & Williams, R. S. The missing memristor found. *Nature* **453**, 80–83 (2008); erratum **459**, 1154 (2009).
4. Kwon, D. H. et al. Atomic structure of conducting nanofilaments in TiO_2 resistive switching memory. *Nat. Nanotechnol.* **5**, 148–153 (2010).
5. Yang, J. J., Strukov, D. B. & Stewart, D. R. Memristive devices for computing. *Nat. Nanotechnol.* **8**, 13–24 (2013).
6. del Valle, J., Ramirez, J. G., Rozenberg, M. & Schuller, I. K. Challenges in materials and devices for resistive-switching-based neuromorphic computing. *J. Appl. Phys.* **124**, 211101 (2018).
7. Zhou, Y. & Ramanathan, S. Mott memory and neuromorphic devices. *Proc. IEEE* **103**, 1289–1310 (2015).
8. Prezioso, M. et al. Training and operation of an integrated neuromorphic network based on metal-oxide memristors. *Nature* **521**, 61–64 (2015).
9. Schuller, I. K. & Stevens, R. *Neuromorphic Computing: from Materials to Systems Architecture* https://science.energy.gov/~/media/ascr/pdf/programdocuments/docs/Neuromorphic-Computing-Report_FNLBLP.pdf (US Department of Energy, Washington DC, 2015).
10. Brockman, J. S. et al. Subnanosecond incubation times for electric-field-induced metallization of a correlated electron oxide. *Nat. Nanotechnol.* **9**, 453–458 (2014).
11. del Valle, J. et al. Electrically induced multiple metal-insulator transitions in oxide nanodevices. *Phys. Rev. Appl.* **8**, 054041 (2017).
12. Zimmers, A. et al. Role of thermal heating on the voltage induced insulator-metal transition in VO_2. *Phys. Rev. Lett.* **110**, 056601 (2013).
13. Stoliar, P. et al. A leaky-integrate-and-fire neuron analog realized with a Mott insulator. *Adv. Funct. Mater.* **27**, 1604740 (2017).
14. Pickett, M. D., Medeiros-Ribeiro, G. & Williams, R. S. A scalable neuristor built with Mott memristors. *Nat. Mater.* **12**, 114–117 (2013).
15. Imada, M., Fujimori, A. & Tokura, Y. Metal–insulator transitions. *Rev. Mod. Phys.* **70**, 1039 (1998).
16. Park, J. H. et al. Measurement of a solid-state triple point at the metal–insulator transition in VO_2. *Nature* **500**, 431–434 (2013).
17. Mazza, G., Amaricci, A., Capone, M. & Fabrizio, M. Field-driven Mott gap collapse and resistive switch in correlated insulators. *Phys. Rev. Lett.* **117**, 176401 (2016).
18. Zhou, Y. et al. Voltage-triggered ultrafast phase transition in vanadium dioxide switches. *IEEE Electron Device Lett.* **34**, 220–222 (2013).
19. Yang, J. J. et al. Engineering nonlinearity into memristors for passive crossbar applications. *Appl. Phys. Lett.* **100**, 113501 (2012).
20. Madan, H., Jerry, M., Pogrebnyakov, A., Mayer, T. & Datta, S. Quantitative mapping of phase coexistence in Mott-Peierls insulator during electronic and thermally driven phase transition. *ACS Nano* **9**, 2009–2017 (2015).
21. Binder, K. Theory of first-order phase transitions. *Rep. Prog. Phys.* **50**, 783 (1987).
22. Gray, A. X. et al. Ultrafast terahertz field control of electronic and structural interactions in vanadium dioxide. *Phys. Rev. B* **98**, 045104 (2018).
23. O'Callahan, B. T. et al. Inhomogeneity of the ultrafast insulator-to-metal transition dynamics of VO_2. *Nat. Commun.* **6**, 6849 (2015).
24. Ramírez, J. G., Sharoni, A., Dubi, Y., Gómez, M. E. & Schuller, I. K. First-order reversal curve measurements of the metal-insulator transition in VO_2: signatures of persistent metallic domains. *Phys. Rev. B* **79**, 235110 (2009).
25. Claassen, J. H., Lu, J. W., West, K. G. & Wolf, S. A. Relaxation dynamics of the metal-semiconductor transition in VO_2 thin films. *Appl. Phys. Lett.* **96**, 132102 (2010).
26. Nag, J., Haglund, R. F. Jr, Payzant, E. A. & More, K. L. Non-congruence of thermally driven structural and electronic transitions in VO_2. *J. Appl. Phys.* **112**, 103532 (2012).
27. Vinokur, V. M., Feigel'man, M. V. & Geshkenbein, V. B. Exact solution for flux creep with logarithmic $U(j)$ dependence: self-organized critical state in high-T_c superconductors. *Phys. Rev. Lett.* **67**, 915 (1991).
28. Le Gallo, M., Krebs, D., Zipoli, F., Salinga, M. & Sebastian, A. Collective structural relaxation in phase-change memory devices. *Adv. Electron. Mater.* **4**, 1700627 (2018).
29. Amir, A., Oreg, Y. & Imri, Y. On relaxation and aging of various glasses. *Proc. Natl Acad. Sci. USA* **109**, 1850–1855 (2012).
30. Béland, L. K., Osetsky, Y. N., Stoller, R. E. & Xu, H. Slow relaxation of cascade-induced defects in Fe. *Phys. Rev. B* **91**, 054108 (2015).
31. Sohn, A., Kanki, T., Sakai, K., Tanaka, H. & Kim, D.-W. Fractal nature of metallic and insulating domain configurations in a VO_2 thin film revealed by Kelvin probe force microscopy. *Sci. Rep.* **5**, 10417 (2015).
32. Sharoni, A., Ramirez, J. G. & Schuller, I. K. Multiple avalanches across the metal-insulator transition of vanadium oxide nanoscaled junctions. *Phys. Rev. Lett.* **101**, 026404 (2008).
33. Wang, S. et al. Ultrafast photo-induced dynamics across the metal-insulator transition of VO_2. *EPL* **118**, 27005 (2017).
34. Zhu, Y. et al. Unconventional slowing down of electronic recovery in photoexcited charge-ordered $La_{1/3}Sr_{2/3}FeO_3$. *Nat. Commun.* **9**, 1799 (2018).

Acknowledgements The development of the materials and devices in this Letter was supported by the Vannevar Bush Faculty Fellowship programme sponsored by the Basic Research Office of the Assistant Secretary of Defense for Research and Engineering and funded by the US Office of Naval Research through grant N00014-15-1-2848. The neuromorphic aspects of this work, including the collaboration between UCSD and CNRS, were supported as part of the Quantum Materials for Energy Efficient Neuromorphic Computing, an Energy Frontier Research Center funded by the US Department of Energy, Office of Science, Basic Energy Sciences under award DE-SC0019273. Part of the fabrication process was done at the San Diego Nanotechnology Infrastructure (SDNI) of UCSD, a member of the National Nanotechnology Coordinated Infrastructure (NNCI), which is supported by the US National Science Foundation under grant ECCS-1542148. J.G.R. acknowledges support from FAPA and Colciencias number 120471250659. J.d.V. and J.T. thank Fundación Ramón Areces for their support with a postdoctoral fellowship. J.d.V. thanks I. Valmianski for helpful discussions.

Reviewer information *Nature* thanks Kristjan Haule, Cheol Seong Hwang and the other anonymous reviewer(s) for their contribution to the peer review of this work.

Author contributions J.d.V., J.T., J.G.R. and I.K.S. conceived and designed the experiment. J.d.V., Y.K. and M.-H.L. fabricated the samples. J.d.V. and P.S. performed the transport measurements with assistance from G.K. The reflectivity measurements were performed by N.M.V. and J.d.V. P.W. did the COMSOL simulations. F.T. and M.J.R. simulated the relaxation dynamics. J.d.V., P.S. and I.K.S. wrote the manuscript. All authors participated in the discussion of the results and corrected multiple iterations of the manuscript.

Competing interests The authors declare no competing interests.

Additional information
Extended data is available for this paper at https://doi.org/10.1038/s41586-019-1159-6.
Supplementary information is available for this paper at https://doi.org/10.1038/s41586-019-1159-6.
Reprints and permissions information is available at http://www.nature.com/reprints.
Correspondence and requests for materials should be addressed to J.d.
Publisher's note: Springer Nature remains neutral with regard to jurisdictional claims in published maps and institutional affiliations.

METHODS

Sample preparation. A 70-nm-thick VO_2 film was grown by reactive sputtering on top of an R-cut (oriented along the (1−102) plane) Al_2O_3 substrate. A 4-mtorr argon/oxygen mix (8% O_2) was used during deposition, and the substrate was kept at 520 °C during the growth and later cooled down at a rate of 12 °C min^{-1}. X-ray diffraction measurements confirmed single-phase growth, textured along ⟨100⟩ for VO_2. Two Ti (20 nm)/Au (30 nm) electrodes were patterned on top of the VO_2 film using electron (e)-beam lithography and e-beam evaporation. A 100-nm gap was left between both electrodes, so electric fields of the order of several tens of megavolts per metre could be generated by applying a few volts. Reactive ion etching was used to electrically isolate all devices from each other. Optical lithography and Ti/Au e-beam evaporation were used to create the transmission line contacts to the nanogaps made by e-beam lithography.

Fast transport measurements. Measurements were carried out in a TTPX Lakeshore cryogenic probe station. The station was equipped with high-speed (20 GHz) probes, with ground/line/ground geometry and 50 Ω characteristic impedance. To avoid reflections (the insulating resistance of the device is in the 10^4 Ω range) a 50-Ω termination to ground was installed before the sample (Fig. 1a). A 240-MHz Tektronix function generator was used to create the voltage pulses and a 50 Ω terminated Tektronix broadband oscilloscope (20 GHz) was used to monitor the current.

Optical reflectivity measurements. Reflectivity during resistive switching was measured in a 10-μm VO_2 gap between two electrodes. The sample was mounted on a Montana C2 S50 Cryocooler to control the temperature precisely. A 660-nm laser was focused down to a 5-μm spot within the VO_2 gap using the optical stage of a Durham Magnetooptics Nanomoke3 system. Note that the insulating state has higher reflectivity for 660-nm light, contrary to what happens for longer wavelengths[35]. The IMT was triggered in the device using 10-mA current pulses of 10 ms, generated by a Keithley 6221 current source. The response time of the current source together with the intrinsic capacitance of the setup yielded a rise time of 30–40 μs, which is at least two orders of magnitude smaller than the observed IMT relaxation dynamics.

COMSOL Multiphysics simulations. To examine electrothermal heating in the device, we used finite-element method (FEM) simulations implemented through COMSOL Multiphysics software. Our model couples electrodynamics and heat transfer physics, and the dimensions of the simulated device are identical to those of the real one. The conductivity of the oxide thin film was fitted to the experimental R–T curve and other material properties were taken from the literature[36]. Special care is needed to acquire a convergent solution because of the temperature-dependent conductivity of the oxide, which changes by orders of magnitude within a few kelvins. Thus, for steady-state simulations, we implemented an iterative method in COMSOL where a constantly damped Newtonian step is taken at each iteration. This ensured that convergence was achieved for our solutions, and successfully reproduced the I–V characteristics of real devices, giving threshold voltages and low-resistance states in the same range as in the experiments. Extended Data Fig. 4a shows the V–I curve of a 100 nm VO_2 nanogap at $T = 325$ K.

For time-dependent simulations, we used the default COMSOL time-dependent solver, which implements the BDF method for time-stepping. These solvers were run until the relative error was less than 10^{-3} for dependent variables, obtaining good agreement with experiments. Extended Data Fig. 4b shows I versus t when 200 ns pulses are applied. Note that a threshold behaviour is found, and characteristic insulator-to-metal switching times of the order of 1–10 ns are obtained.

Although COMSOL does not compute features such as relaxation or domain formation, it provides an excellent average approximation of the timescales, lengths, voltages and temperatures associated with the resistive switching process[37].

Relaxation dynamics simulation. We used a 2D resistor network of 100 × 50 sites. Each site of the network represents a small (nanoscale) region of the physical system[18], but large enough so that its electronic state is well defined. Each site is assumed to be in one of two possible electronic states: Mott insulator (MI) or correlated metal (CM), with associated high and low resistive values, respectively. The electrodes are assumed to be perfect metals (that is, to have zero resistance). In analogy to the actual experimental setup, the resistor network is connected to a voltage source and a load resistor (Extended Data Fig. 5a). This resistor mimics contact and wire resistances and is key to avoid current runaway.

To model the thermally driven first-order transition in VO_2, we used a local free energy functional of a Landau-type expansion. On the basis of previous theoretical studies[38], we adopt the free energy (f):

$$f(\eta) = h\eta + p\eta^2 + c\eta^4$$

where η is the order parameter, $h = h_1 \times \frac{T - T_C}{T_C} + h_2$, $p = p_1 \times \frac{T - T_C}{T_C} + p_2$, T is the temperature, $T_C = 340$ K is the critical temperature, and h_1, h_2, p_1, p_2 and c are constants. Extended Data Fig. 5b shows this functional for three different temperatures: above, below and at the transition temperature. Two distinct energy minima appear for all three temperatures, as expected in first-order phase transitions. This resistor network allows us to simulate properly the first-order dynamics of the IMT. Extended Data Fig. 6a shows the resistance of the network as a function of the temperature, where hysteresis and phase coexistence are clearly visible.

To simulate the transport dynamics of the system, we proceed as follows. Initially, all cells are assumed to be in the MI state. Then, an external voltage $V(t)$ is applied. At every time step t_i the full resistor network circuit is solved, obtaining all the local currents and voltage drops. The local temperatures are updated using the heat equation through the discrete Laplacian approximation:

$$c_h(\partial T(x,y)/\partial t) = p(x,y) - \kappa(5T(x,y) - \Sigma_{\text{First neighbours}} T_i - T_B)$$

where c_h is the heat capacity of each cell, $p(x,y)$ is the dissipated power, and κ is the thermal conductance. The $\Sigma_{\text{First neighbours}}$ operator performs a summation over the first neighbours of each cell. Each cell exchanges heat with its four neighbours in the network and with the substrate at constant temperature T_B (we assume a planar structure of the device). The cells at the top, at the bottom and on the lateral borders exchange heat with three neighbours and a virtual cell at constant temperature T_B.

At each time step, the temperature of each cell is updated and the local energy landscape is recalculated. According to the new energy landscape, each cell in the network can undergo a local Mott transition (from MI to CM or vice versa), with a probability P given by the free energy barrier Δf ($P = e^{-\Delta f/kT}$), where f is the free energy defined above. The cell will switch into the metallic state if Joule heating is high enough. After the state of all cells is updated with the corresponding probability, the simulation moves to the next discrete time step and the process is repeated. Extended Data Fig. 6b shows how this method allows us to reproduce the voltage-triggered IMT. We must say that, although we chose Joule heating as the triggering mechanism, similar results could be obtained if the triggering was purely caused by the electric field[12].

When the sample becomes conducting, part of the voltage drops across the load resistor, reducing the voltage across the sample electrodes. This creates 'S'-shaped I–V_{Sample} curves, as shown in Extended Data Fig. 6c. Ridley[39] proposed that such a shape could cause a dynamic instability and lead to the formation of current density or electric field domains across the sample[40]. In our model, such domain formation is clearly visible as current density filaments connecting both electrodes (see Fig. 4).

After the voltage pulse and once the device cools down, the different cells can return to their original insulating state by crossing the energy barrier. This allows us to simulate the relaxation dynamics shown in Fig. 4. As the temperature gets closer to T_C the energy barrier increases, leading to a slowing down in the relaxation dynamics similar to the experiments. Extended Data Fig. 6d shows $\tau_{50\%}$ versus temperature, and a clear divergence can be seen at 340 K.

We must note that our simulations do not reproduce an important feature seen in the experiments: the persistence of the effect for several decades in time. In the main text, it is argued that such power-law decay is characteristic of collective relaxation processes. Extended Data Fig. 6e shows the probability of firing the transition with a pulse 0.6 $V_{Threshold}$ as a function of delay time τ: all the relaxation takes place within a narrow time window. This discrepancy with the experiments is to be expected, as in our simulations each cell is independent from the others, and there is no coupling to induce collective dynamics and long-lived domains. Relaxation is exponential instead of following a power law. However, this does not affect the main conclusion of the simulations: residual domains can indeed cause subthreshold firing and explain why the device keeps a memory of a previous firing event. The simulated triggering/retriggering process can be visualized in the Supplementary Video.

Discussion on frequency discrimination. The memory effect described in the main text could be used to implement new functionalities in oxide electronics. Here we demonstrate phase-transition-based frequency discrimination. The top panels in Extended Data Fig. 3a show two sequences of applied voltage pulses in one of our VO_2 devices. Both sequences consist of an initial super-threshold pulse followed by multiple subthreshold pulses separated either by 10 μs or 5 μs. The bottom panels show the current response as a function of time. In the case of 10 μs separation, the device only fires once more after the first pulse triggers the IMT. The situation is very different when the separation is reduced to 5 μs: the separation between pulses is short enough to continue refreshing the memory, resulting in continuous subthreshold firing. This opens the possibility of using VO_2 devices as frequency discriminators: if the frequency is high enough, the memory will be refreshed at each pulse and the signal will go through. Extended Data Fig. 3b shows the attenuation of sinusoidal signals through a 50 Ω load resistor in series with the device, as a function of frequency. A clear and sharp (almost 40 dB) high-pass filter characteristic is observed. Notably, the cut-off frequency is amplitude-dependent, which gives the possibility of tuning the device by adjusting the intensity of the incoming signal. This feature is to be expected, as the memory time depends on the subthreshold pulse amplitude (Fig. 2c).

So far, filtering and frequency discrimination has always been implemented using resonant structures or LC circuits[41]. The wavelength size in the first case

and the capacitor size in the second limit the scalability of these devices, which are normally larger than 100 μm. Our results show frequency discrimination based on the intrinsic dynamics of a phase transition. These are mostly geometry independent, and might allow radio-frequency circuitry to be shrunk to the nanoscale.

Data availability

All the data supporting the claims and figures of this Letter are available from the corresponding author upon reasonable request.

Code availability

The code used in the simulations supporting this Letter is available from J.d.V. (jdelvallegranda@ucsd.edu) or M.R. (marcelo.rozenberg@u-psud.fr) upon reasonable request.

35. Qazilbash, M. M. et al. Mott transition in VO_2 revealed by infrared spectroscopy and nano-imaging. *Science* **318**, 1750–1753 (2007).
36. Kizuka, H. et al. Temperature dependence of thermal conductivity of VO_2 thin films across metal–insulator transition. *Jpn. J. Appl. Phys.* **54**, 053201 (2015).
37. Valmianski, I. et al. Origin of the current-driven breakdown in vanadium oxides: thermal versus electronic. *Phys. Rev. B* **98**, 195144 (2018).
38. Kotliar, G., Lange, E. & Rozenberg, M. J. Landau theory of the finite temperature Mott transition. *Phys. Rev. Lett.* **84**, 5180–5183 (2000).
39. Ridley, B. K. Specific negative resistance in solids. *Proc. Phys. Soc.* **82**, 954 (1963).
40. Kumar, S. & Williams, R. S. Separation of current density and electric field domains caused by nonlinear electronic instabilities. *Nat. Commun.* **9**, 2030 (2018).
41. Young, P. H. *Electronic Communication Techniques* 3rd edn 360–374 (McMillan Publishing, New York, 1994).

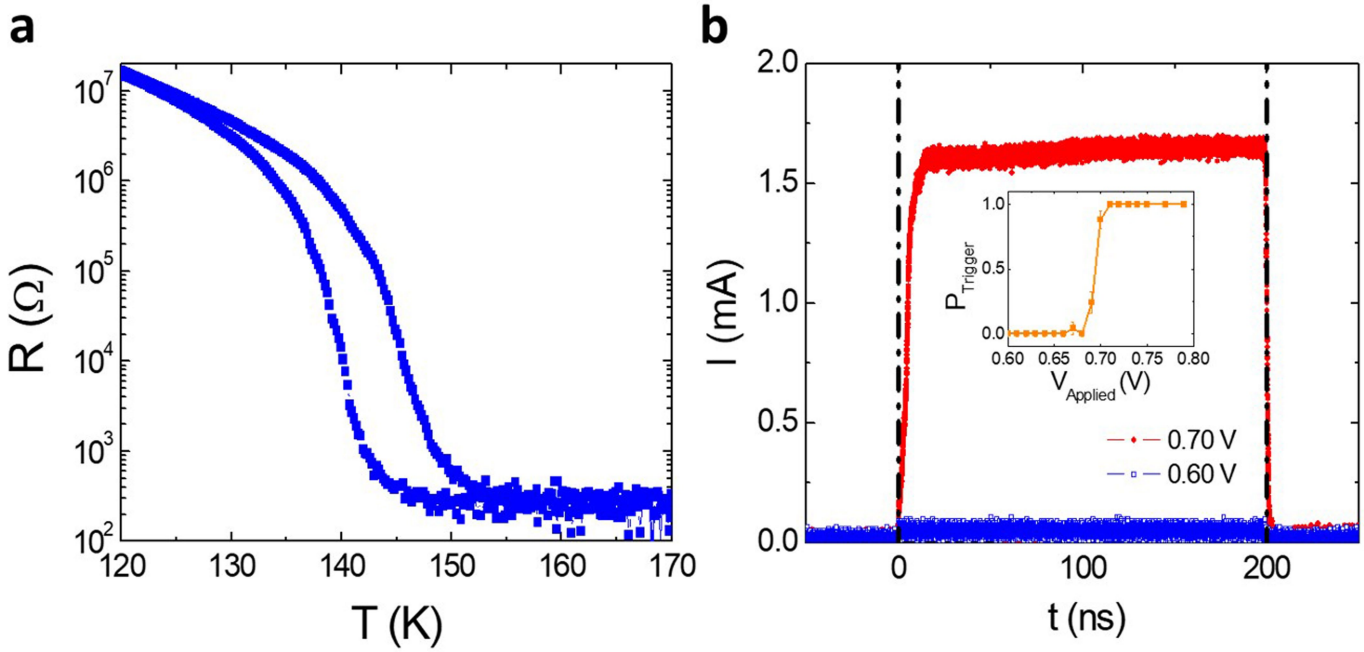

Extended Data Fig. 1 | Temperature- and voltage-induced IMT in V_2O_3. a, Resistance versus temperature in a V_2O_3 nanodevice. Both the heating and cooling branches are shown. **b**, Main panel, current versus time when a 200-ns voltage pulse is applied to the device at 132 K. Results for two voltage amplitudes are shown: subthreshold (0.6 V; in blue) and super-threshold (0.7 V; in red). Inset, the probability of firing the IMT ($P_{Trigger}$) as a function of the voltage amplitude ($V_{Applied}$). This probability was obtained by observing how many times the IMT was triggered in 100 pulses. The error bars were calculated using the standard deviation of the binomial distribution.

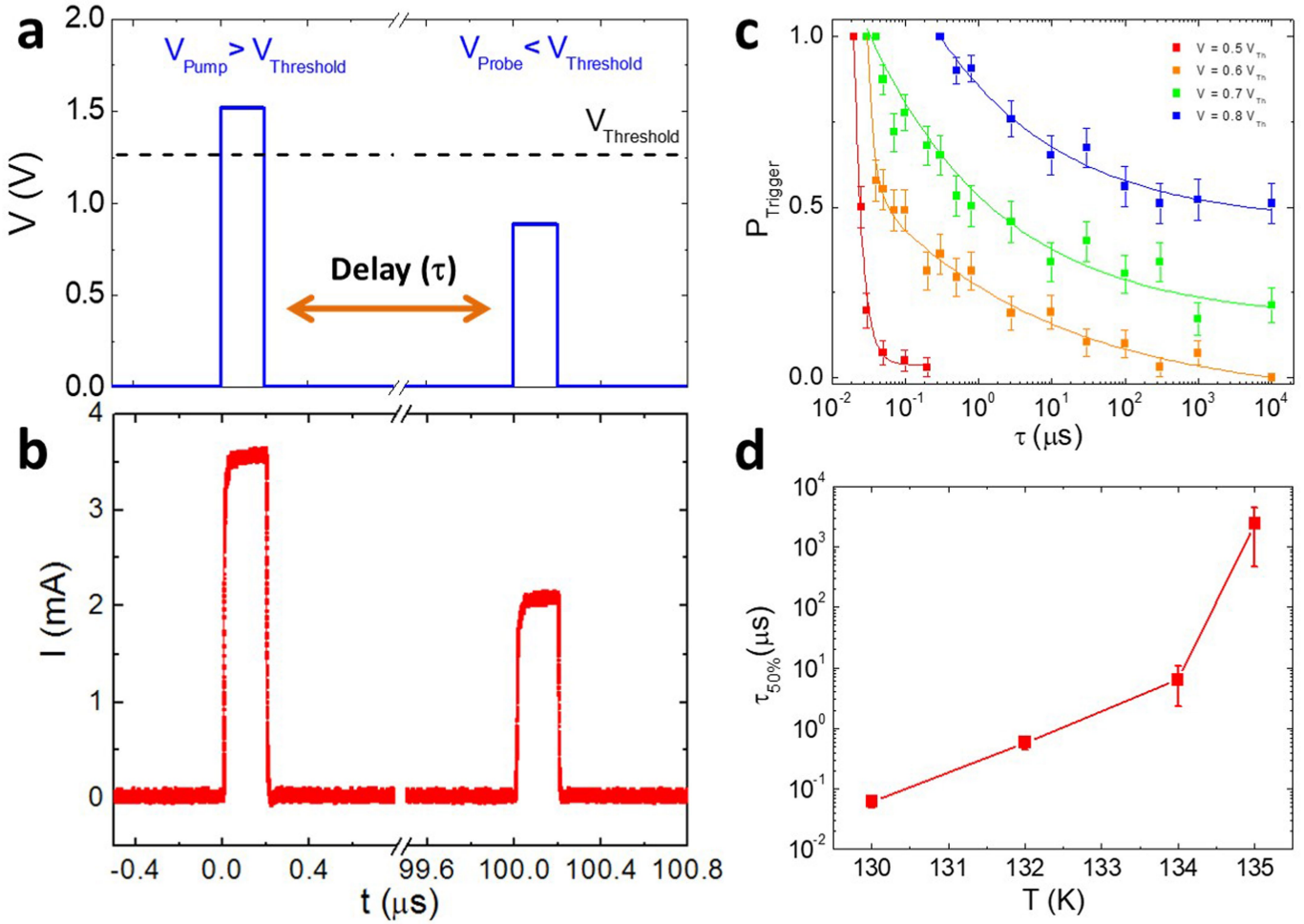

Extended Data Fig. 2 | Subthreshold firing and memory effect in V_2O_3. **a**, Applied voltage as a function of time. The pump–probe procedure consists of a super-threshold pulse first applied to trigger the IMT, followed, after a delay time τ, by a subthreshold probe pulse. The dashed line shows $V_{\mathrm{Threshold}}$. **b**, Current versus time at $T = 130$ K when the voltage shown in **a** is applied with a delay $\tau = 100$ μs between the pulses. The transition is triggered in both cases. **c**, Probability that the probe pulse will trigger the IMT (P_{Trigger}) as a function of τ, at $T = 130$ K. This probability was obtained by observing how many times the IMT was triggered in 100 pulses. The error bars were calculated using the standard deviation of the binomial distribution. P_{Trigger} is plotted for different V_{Probe} amplitudes: $0.5V_{\mathrm{Th}}$, $0.6V_{\mathrm{Th}}$, $0.7V_{\mathrm{Th}}$ and $0.8V_{\mathrm{Th}}$ (see key; $V_{\mathrm{Th}} = V_{\mathrm{Threshold}}$). Solid lines are fits to curves of the type $\alpha t^{-\beta} + \gamma$, where α, β and γ are fitting parameters obtained by the least-squares method. **d**, Delay time $\tau_{50\%}$, at which the firing probability is 50%, plotted against T for a pulse with amplitude 0.6 $V_{\mathrm{Threshold}}$. $\tau_{50\%}$ was calculated using the fitting curves shown in **c**. Error bars were derived by uncertainty propagation, using the standard error of the fit.

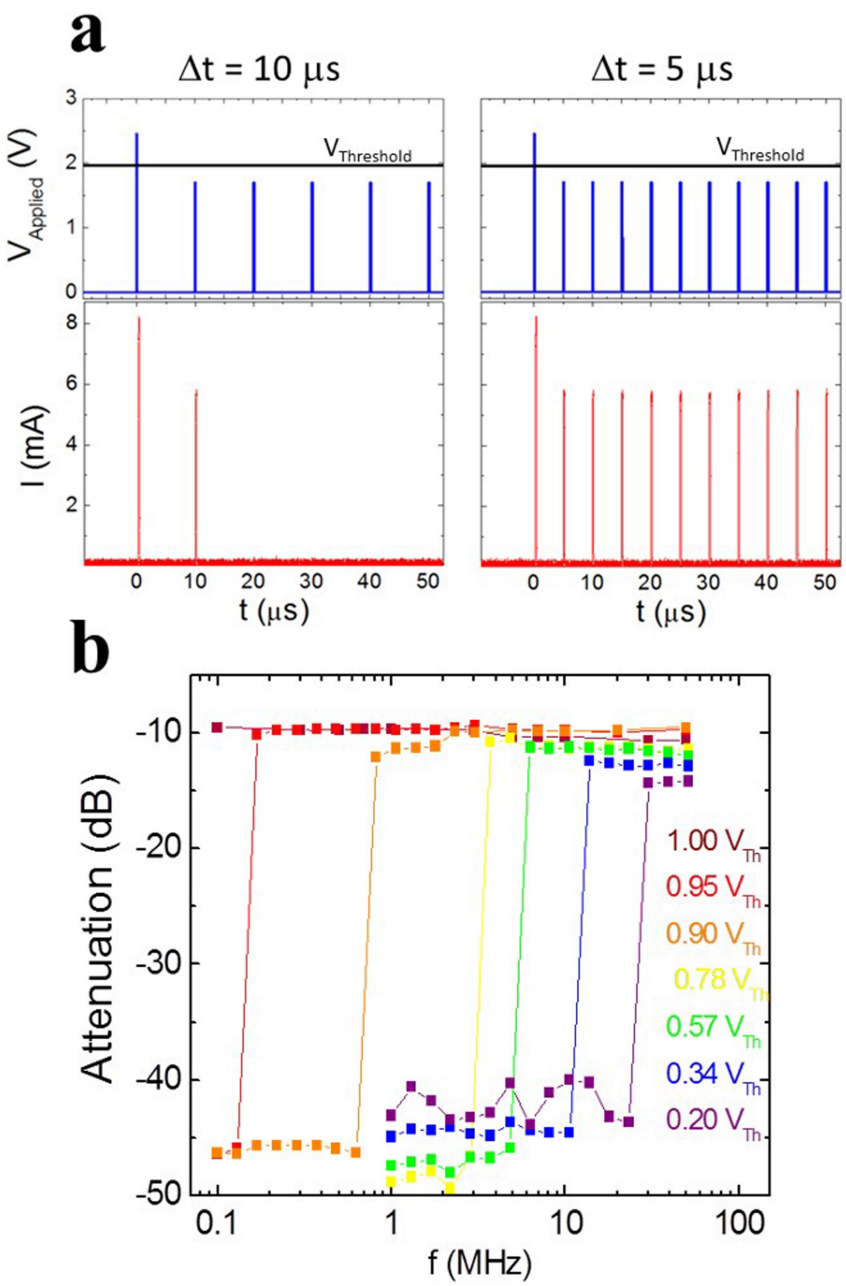

Extended Data Fig. 3 | Frequency discrimination using subthreshold firing in VO_2. a, Top panels, voltage pulses applied to the gap versus time. The first super-threshold pulse is followed by a series of subthreshold voltages separated by 10 μs (left) or 5 μs (right). Bottom panels, current versus time when the pulses are applied. Note that when the pulse separation is 5 μs, each voltage pulse refreshes the memory of the device, allowing for repeated subthreshold firing. The temperature was 330 K. **b**, Attenuation of a sinusoidal signal through a nanodevice as a function of the signal frequency. The output voltage was measured on a 50-Ω load resistor. Several signal amplitudes are shown (see key; $V_{th} = V_{Threshold}$). The device was initiated with a super-threshold voltage pulse before the sine signal was sent. The temperature was 325 K.

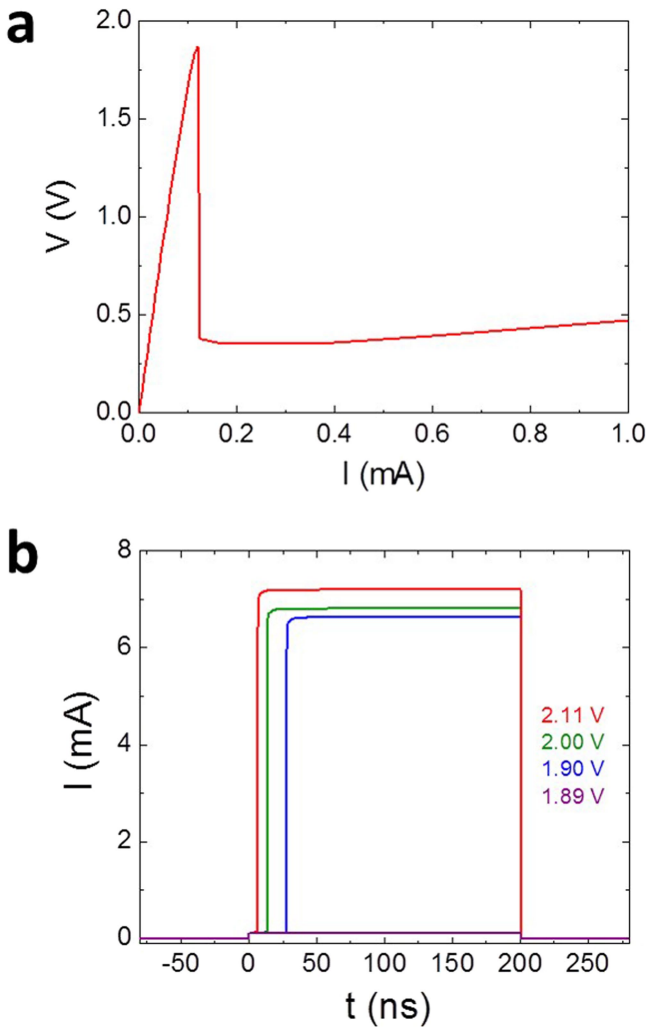

Extended Data Fig. 4 | COMSOL Multiphysics simulations. a, Voltage versus current in a 100-nm VO_2 nanogap. A 260-Ω load resistance was used to mimic contact resistance in the probe station. Base temperature in the simulation was 325 K. **b**, Current versus time when 200-ns voltage pulses of different amplitude are applied at $t = 0$ ns. The simulation temperature was 325 K. Different voltage amplitudes are used: 1.89 V ($< V_{Threshold}$), 1.90 V, 2.00 V and 2.11 V. Note that the delay times are of the order of nanoseconds or tens of nanoseconds, similar to the experimental results.

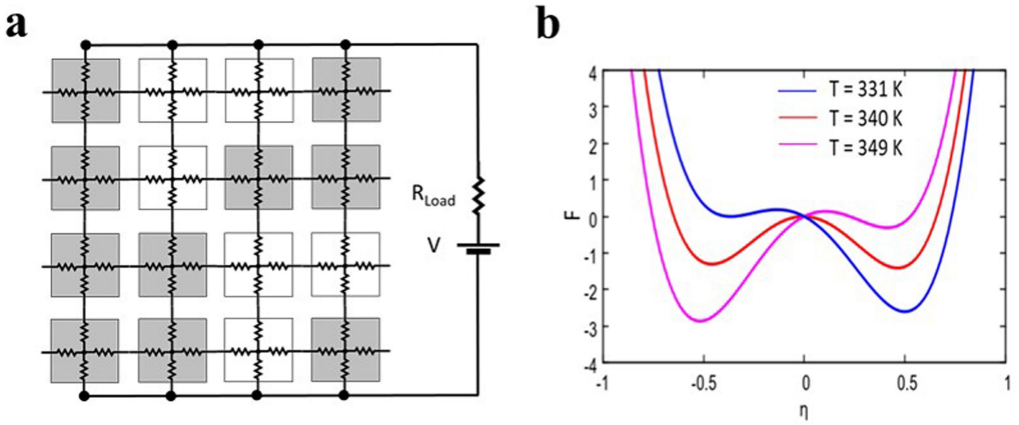

Extended Data Fig. 5 | Landau-type model of resistive switching. **a**, Schematic representation of the resistor network used to model VO_2. Each node of the network is connected to its nearest neighbours by a resistor. The value of the resistor depends on the local state: metallic (dark grey) or insulating (white). A load resistor (R_{load}) is placed in series with the network. **b**, Free energy (F) as a function of the order parameter η for three different temperatures (331 K, 340 K and 349 K). The node is metallic if $\eta < 0$ and insulating for $\eta > 0$.

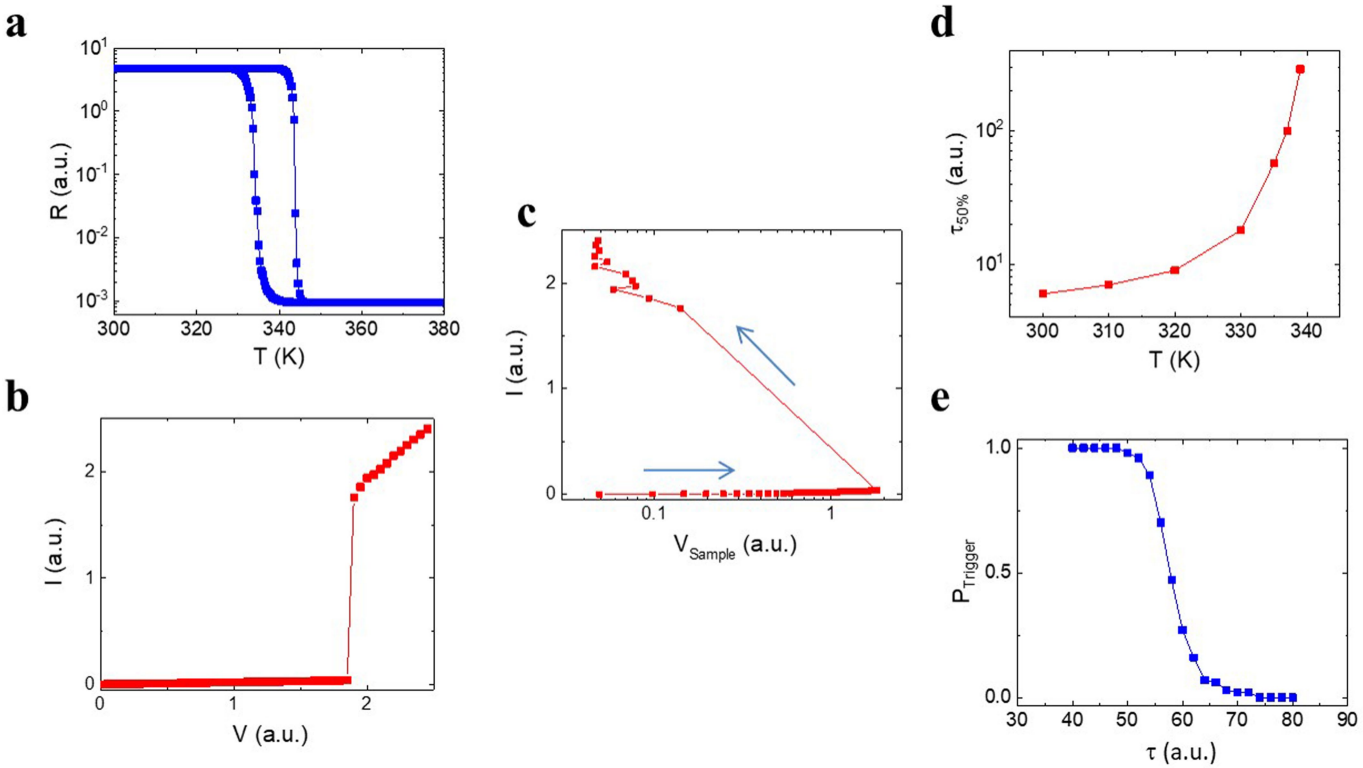

Extended Data Fig. 6 | Simulation results. a, Resistance (R) versus temperature (T) of the simulated network. **b**, Simulated current (I) versus voltage (V) at $T = 330$ K. **c**, Simulated current (I) versus V_{Sample} at $T = 330$ K. **d**, $\tau_{50\%}$ versus temperature. $\tau_{50\%}$ is defined as the time at which there is a 50% probability of triggering the transition with a voltage pulse amplitude of 0.6 $V_{\mathrm{Threshold}}$, using a pump–probe protocol similar to the experiments. **e**, Probability (P_{Trigger}) that a probe pulse with amplitude 0.6 $V_{\mathrm{Threshold}}$ will trigger the transition as a function of the separation time between pulses (τ). The simulation temperature was 335 K.